Mechanism of visible-light-driven photocatalytic degradation of endosulfan pesticide by gold nanoparticles

Environmental Research Communications

PAPER

Mechanism of visible-light-driven photocatalytic degradation of endosulfan pesticide by gold nanoparticles

Puja Goel[1] **and Manju Arora**[2]

[1] Physics Department, College of Basic Sciences and Humanities, G B Pant University of Agriculture and Technology, Pantnagar, Uttarakhand, India

[2] CSIR- National Physical Laboratory, Dr K.S. Krishnan Marg, New Delhi 110012, India

E-mail: pujagoel@gmail.com

Keywords: GNPs, organochlorine

OPEN ACCESS

RECEIVED
18 March 2020

REVISED
7 July 2020

ACCEPTED FOR PUBLICATION
9 July 2020

PUBLISHED
21 July 2020

Abstract

Spherical shaped gold nanoparticles (GNPs) of size around ~9 nm were successfully used for photocatalytic degradation of hazardous endosulfan (ES) pesticide. GNPs absorb sunlight at ambient condition in aqueous medium to enhance localized surface plasmon resonance (LSPR) which initiate hydrolysis, oxidation and reduction chemical reactions for the mineralization of ES molecules. Infrared transmittance spectra of GNPs treated ES solutions revealed formation of amorphous carbon and hydrocarbon as final reaction products indicating the nearly complete mineralization of ES as evidenced from their TEM images also. The disappearance of chloro carbon and sulphite functional groups peaks of ES in IR transmittance spectra confirmed their degradation. TEM images also support the optical absorption spectra consisting of inter-band and LSPR bands pertaining to individual and clustered GNPs ensembles. The redshift in LSPR absorption peak positions along minor and major axis of clustered GNPs ensembles is attributed to the change in GNPs polarizability on interaction with the electric component of visible light. The chemical reaction pathway for ES molecule degradation by the photocatalytic GNPs has been proposed in the light of inferences drawn from TEM images, IR transmittance and optical absorption spectra.

Introduction

Photocatalysts as clean and green sources play a vital role in meeting the demand of pollution free environment by the decontamination of life saving natural resources like soil, water, air and also in energy related applications. Extensive research is going on the development of new economically efficient and advanced photocatalytic materials suitable for maximum energy absorption from visible region of solar spectrum [1–10]. Studies were reported on both homogeneous and heterogeneous photocatalytic materials for the oxidation reactions. Hydrogen peroxide (H_2O_2), ozone (O_3), Fenton reagent, sodium hypochlorite (NaOCl) are categorized under homogeneous photocatalytic materials [1] and used either individually or in combination with light to undergo oxidation reaction for the degradation of pollutants. Semiconducting II–VI metal oxides/sulphides e.g. TiO_2 [2], ZnO [3], ZnS [4]; CdS [4], WO_3 [5], Bi_2O_3 [6], Bi_2S_3 [7], SnO_2 [8], MnO_2 [9] and Au/Ag/Cu metal nanoparticles supported on different metal oxides [10] etc are characterized under the heterogeneous photocatalysts. They utilizes UV and/or visible solar radiation to generate variety of reactive oxygen species for photocatalytic oxidation. These metal oxides/sulphides exhibit best efficiencies under UV-light irradiation because of their wide energy band gap. In addition to these photocatalysts, work on new nanocomposite materials suitable for visible region absorption is also reported [11–15]. Some of those are $Bi/BiVO_4$, $g\text{-}C_3N_4/SmVO_4$ [11], $Sr_{0.25}Bi_{0.75}O_{1.36}$ [12], $CeO_2/SnO_2/rGO$ [13], Ag_3PO_4 [14] and $Fe_2(MoO_4)_3$ [15]. However, these composites have disadvantages such as limited visible-light absorption, swift charge recombination and poor stabilities which restricts their usage in different applications. Recently, the study of optical and catalytic properties of GNPs as photocatalyst has attracted researchers owing to its capability of simultaneously absorbing visible and ultraviolet light from solar spectrum. The LSPR signal of noble metals of

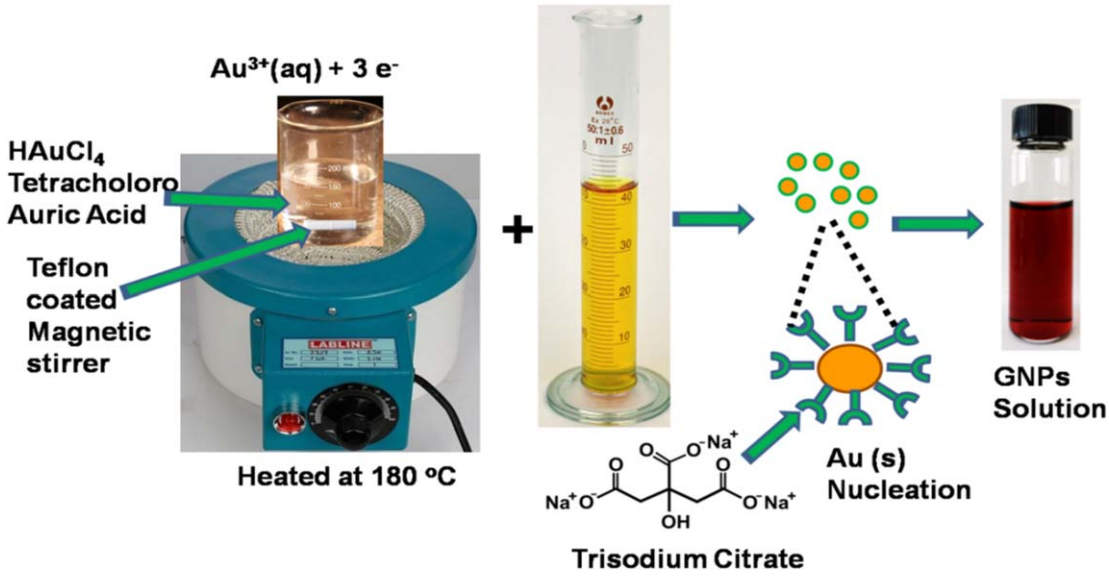

Figure 1. Schematic of GNPs synthesis by citrate route.

size more than 5 nm absorbs light in the visible region [16–20] and also acts as an electron trap for photoinduced electrons [21]. The intensity of plasmonic band is sensitive to the morphology, dielectric constant of dispersing medium and electronic interactions involved in stabilizing ligands and nanoparticles [19]. In nobel metals, photocatalytic reaction, light absorption and activation of reactants take place simultaneously which enhances their light harvesting and thermal energy absorption capacity i.e. photocatalytic quantum efficiency to initiate chemical reactions [20]. In GNPs, LSPR effect couples with sunlight to generate high energy conduction electrons at the surface of the nanoparticle to initiate chemical reaction with molecules adsorbed on their surface [19, 20, 22–27]. The excited electrons and enhanced electric field of GNPs convert solar energy into chemical energy by the photon-driven photocatalytic reaction. It implies that during photocatalysis, light harvesting from sunlight and chemical reaction with adsorbed species/molecules on noble metal NPs surface is going on side-by-side. The strong visible light absorption, recyclability and large surface area to volume ratio of GNPs have proved them to be a suitable candidate for photocatalytic reaction. Current investigation aims to exploit the photocatalytic activity of GNPs for mineralization of hazardous organochlorine pesticide ES. Long environmental life span and deadly health effects of ES and its metabolites have encouraged the researchers for pursuing easy and economic detoxification pathways from the environment. Different bulk and nanomaterials have been used for their mineralization via hydrolysis, oxidation and reduction reactions e.g. carbon based nanomaterials, semiconducting oxides, magnetic oxides and nobel metals nanoparticles [22–25, 28, 29]. In the present work, different concentrations of ES are treated with GNPs solution. The final reaction products were examined by TEM, UV–Vis and FTIR techniques to confirm the mineralization of ES molecules. The mechanism of ES degradation is discussed in the light of photocatalytic activity of GNPs.

Experimental

Synthesis of GNPs

The colloidal solution of GNPs were synthesized by the reduction of Tetra-Chloro Auric Acid (TCAA) (CDH Make, AR grade) via Turkevich method [30]. The details of synthesis process have already been described in P. Goel and M. Arora [26]. 150 ml of 0.5 mM TCAA (2% w/v) and 15 ml of 38.8 mM sodium citrate (3% w/v) solutions were prepared in double distilled water in separate volumetric flasks. The magnetically stirred TCAA solution was heated at 180 °C on hot plate then 15 ml sodium citrate solution was swiftly transferred to it. Resulting solution after 5 min turned slightly bluish and by the end of the reduction process i.e. within 20 min, colloidal gold nanoparticle solution of brilliant wine red color was obtained. The schematic of the synthesis procedure is shown in figure 1.

To explore the degradation of organochlorine ES via photocatalytic GNPs, different concentration of ES solutions ranging from 1 ppm to 50 ppm (i.e. 1, 5, 10, 20, 50 ppm) were prepared in 2-Propanol (HPLC and Spectroscopy grade, CDH Make) by dissolving technical grade endosulfan flakes. Successively, 5 ml of each from 1 ppm to 50 ppm ES solutions were reacted with 0.5 ml GNPs suspension. The morphological details of as

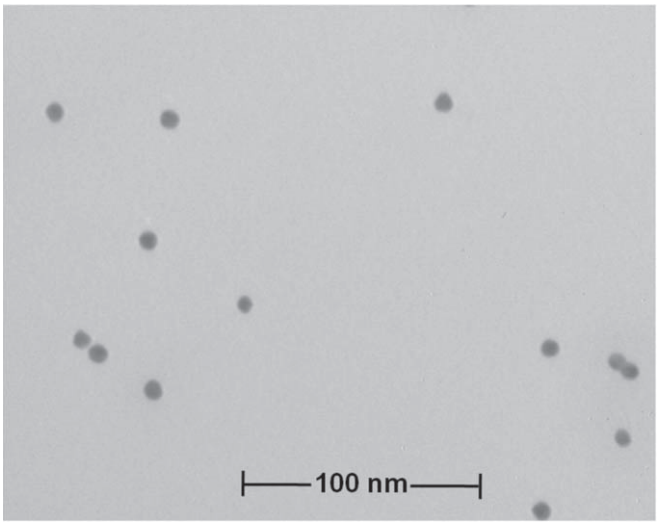

Figure 2. TEM of GNPs at 200 k Magnification.

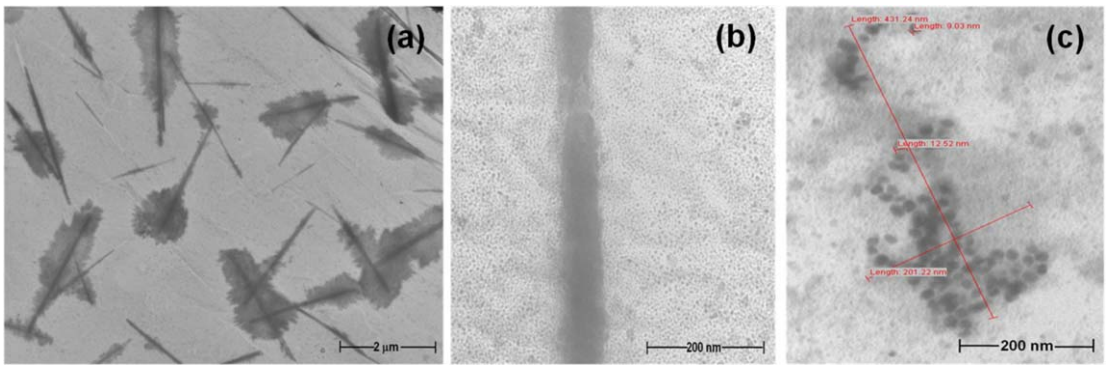

Figure 3. (a) TEM images of 100 ppm ES: GNPs sample at 2 μm scale showing rods as well as floral petal structures (b) Zoomed in version of 'a' at 200 nm scale exhibiting agglomeration of GNPs in rod shape and amorphous carbon particles (c) agglomeration of GNPs as bigger ensembles.

prepared GNPs and GNPs treated ES solution reaction product are inferred from Transmission Electron Microscopy (TEM) images of dried filtrate scanned on JEOL-TEM (1011) microscope. The optical absorption spectra of pure and treated samples were recorded in 200–1000 nm range by using Shimadzu make UV–Vis spectrophotometer (Model: UV-2401 PV). IR transmittance spectra of ES, GNPs and final treated solutions were recorded in 4000–500 cm^{-1} region on M/S Bruker make, ALPHA T model FTIR spectrophotometer at ambient temperature.

Results and discussion

TEM analysis

Figures 2 and 3(a)–(c) present TEM images of as synthesized GNPs and 100 ppm ES solution after reaction with GNPs respectively. The pure GNPs exhibit uniform distribution of spherical shaped nanoparticles with very narrow size distribution in ~8.50 $\pm$ 0.50 nm range. In ES:GNPs sample the images were recorded at different locations under different magnifications. In figure 3(a) the image indicates the formation of long rods (of length in the range of ~1.5 to 3.5 μm) as well as flower petal structure which are randomly distributed. It can also be seen that these rods have grey color patches around them which seem to comprise of ultrafine particles. A 'zoomed in' version of figure 3(a) is shown in figure 3(b) at 200 nm scale which exhibits agglomeration of GNPs in rod shape and ultra fine amorphous carbon particles all over the place.

In figure 3(c), the agglomeration of GNPs in rod, floral petal and feather shaped structures with ultrafine particles are clearly visible in 200 nm scale. These agglomerated structures encourage localized surface plasmon

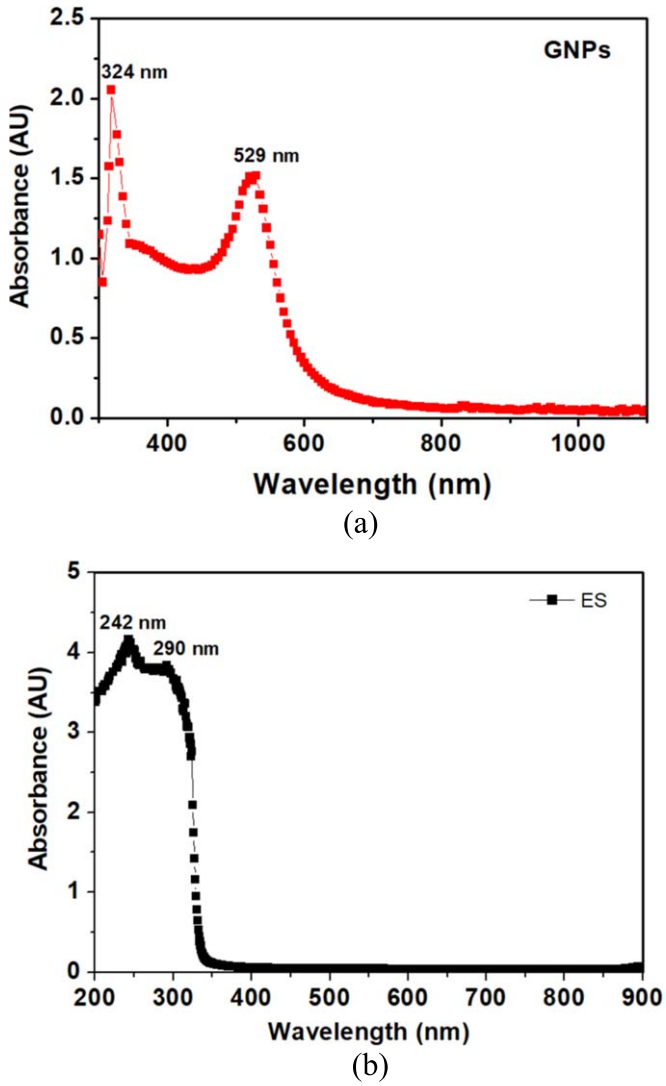

Figure 4. (a) UV– Vis spectra of GNPs suspension. (b) UV–Vis spectra of ES.

resonance in visible region and photocatalytically produced hot electrons and holes initiate hydrolysis, oxidation and reduction chemical reaction for the degradation of ES pesticide into non-hazardous products [19, 20, 27].

UV–Vis spectroscopy studies

Optical absorption spectrum of as-prepared GNPs of ~9 nm size derived by citrate route of ruby red wine colour solution (figure 4(a)) exhibit absorption peaks in UV and visible region at 324 nm and 529 nm due to the inter-band electrons transition from 5d (valence) to 6sp (conduction) levels whereas the strong absorption at 529 nm in as prepared GNPs is due to the LSPR transitions arising from 6sp electrons transition to conduction band [16, 18, 31]. LSPR peak appears due to the absorption of visible light because in small nanoparticles momentum conservation is not required. This fact is further supported by TEM image of GNPs in which uniform dispersion of spherical shaped nanoparticles without any agglomeration is clearly visible. Absorption Spectra of ES with absorption peaks at ~242 and 290 nm is shown in figure 4(b). In figure 5, the absorption spectra of 0.5 ml GNPs solution treated ES (5 m.l. of each 01 ppm–50 ppm ES) are presented and positions of different peaks obtained in the spectra are listed in table 1. The interband and LSPR transition peaks are observed in 350–360 nm and 530–545 nm regions respectively. While the strong and weak peaks observed in 655–695 nm and 985–995 nm pertain to SPR transitions of minor and major axis of ellipsoidal shaped structures of aggregated GNPs ensembles respectively. The redshift in LSPR peak positions as compared to pure GNPs is due to change in GNPs polarizability on interaction with the electric component of visible light and hence confirm the aggregation of small and big sized GNPs clusters. The changes in these peaks intensity reveal the decrease in the availability of active sites i.e. lesser number of individual spherical shaped GNPs in the final reacted solution due to aggregation of GNPs. TEM images of these solutions support these results and exhibit different cylindrical/rod, floral petals and feather shaped structures of GNPs aggregates. The small aggregates are an assembly of three/four GNPs and

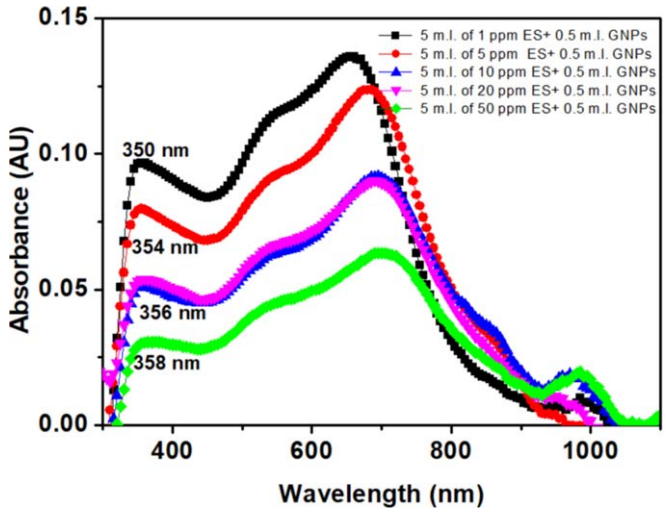

Figure 5. UV–Vis spectra of GNPs treated ES solutions in 1 ppm–50 ppm range.

Table 1. Absorption Peak positions of 0.5 ml GNPs solution treated ES (5 ml of each 01 ppm–50 ppm ES).

	Peak position (nm)			
Sample	1st peak	2nd peak	3rd peak	4th peak
01 ppm 5 ml ES : 0.5 ml GNPs	350	542	657	986
05 ppm 5 ml ES : 0.5 ml GNPs	354	536	681	984
10 ppm 5 ml ES : 0.5 ml GNPs	356	534	684	985
20 ppm 5 ml ES : 0.5 ml GNPs	356	532	689	974
50 ppm 5 ml ES : 0.5 ml GNPs	358	530	693	994

bigger ensembles have a large number of GNPs which are arranged in cylindrical/rod, floral petals and feather shaped structures. The systematic variation in solution colour change is observed i.e. from wine red to pink to violet to purple and finally to light blue as the reaction proceeds between GNPs and different concentration ES solutions. The colour gradient with ES concentrations is clearly apparent with naked eyes [26].

FTIR spectroscopy

The non-destructive infrared spectroscopy has been widely used for the analysis of structure by tentatively assigning observed peaks pertaining to different bonding groups present in materials [32–40]. In this work, GNPs, endosulfan (ES) and GNPs treated ES solutions in varied concentrations were characterized by IR transmittance spectra recorded in 4000–500 cm^{-1} region at ambient temperature. This inferred information has been used for proposing the reaction mechanism for the degradation of ES by photocatalytic GNPs. Technical grade ES used in the present investigations, is a mixture of 70% alpha and 30% beta isomers having chemical structures as presented below in figure 6.

ES has cyclohexadiene as skeletal ring on which out of 6 chlorine, 4 (labelled as 2a, 2b, 3a and 3b) are bonded in-plane at 6, 7, 8, 9 position of cyclohexadiene ring and the remaining 2 Cl (1a, 1b) at 10 position above ring structure, 6 H are present at 1, 5, 5a, 6, 9, 9a positions, methano group at 6, 9 position and 2,4,3-benzodi-oxathiepin-3-oxide of sulphite (SO_3) group is bonded either below or above the hexa-chloro-cyclohexadiene ring.

IR transmittance spectra of pure ES and GNPs exhibit characteristic vibrational peaks pertaining to adsorbed moisture and different functional groups present as discussed in our earlier work [26]. IR transmittance spectra of GNPs reacted with 1 ppm, 5 ppm, 10 ppm, 20 ppm and 50 ppm ES concentration solutions recorded in 4000–500 cm^{-1} region are presented in figure 7. The variations in peak positions and intensity of different functional groups are discussed in detail in the forthcoming sections:

C–H stretching region

ν C–H stretching vibrations of hydrocarbon and hydrogenated amorphous carbon appear in 3000–2800 cm^{-1} region. In ES, the asymmetric (ν_{as}) and symmetric (ν_s) stretching modes of $-CH_3$ group are obtained at 2971 and

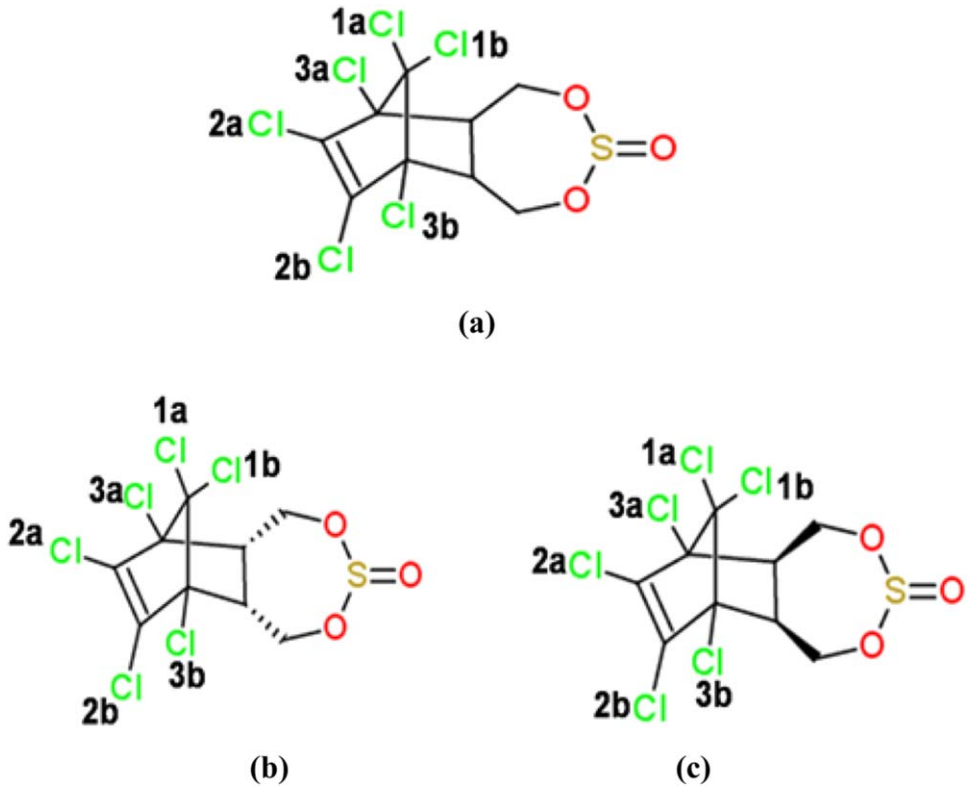

Figure 6. Chemical Structure of (a) Endosulfan (b) α-Endosulfan and (c) β-Endosulfan.

2886 cm^{-1} respectively and ν_{as} CH_2 stretching vibration at 2933 cm^{-1}. The $-CH_2$ stretching modes are stronger than $-CH_3$ stretching modes. However, in ES/GNPs samples, reverse trend is observed, i.e. $-CH_2$ stretching mode intensity is weaker than $-CH_3$ stretching modes. This suggests the conformational sensitivity of $-CH_2$ groups with some of them in *gauche* configuration [41]. This indicates the formation of amorphous phase in the ES:GNPs solution as seen in the TEM micrographs also.

CH_3 bending region

In ES, medium intensity δ (CH_2) peak is observed in 1500–1450 cm^{-1} region as broad band with three components at 1482, 1464 and 1452 cm^{-1} which shows the weak side-by-side interaction between chains to ease charge transfer and chain motion in ES solution [42–44]. The component at 1482 cm^{-1} arises from C–C skeletal vibrations of *trans*conformational chains. While, 1464 cm^{-1} and 1452 cm^{-1} components are tentatively assigned as of CH_3 bending asymmetry mode of partially ordered chain structure and combination mode of *gauche* defects with asymmetric deformation of the terminal CH_3 group of ES molecules [45–47] respectively. In GNPs treated solutions, this peak appears at 1468 cm^{-1} with loss in intensity due to ES degradation and aggregation of GNPs into different size ensembles. These results are supported by TEM images showing small clusters, chain and petal or floral shaped GNPs ensembles and visible change in solution colour initially from wine red to finally light sky blue.

CH_2 wagging region

The characteristic CH_2 wagging modes of *gauche* conformation [34] is obtained as medium intensity band at 1373 cm^{-1} in ES and as doublet band with maxima at 1379 and 1364 cm^{-1} in GNPs:ES solution. It means methyl groups exist in gem- or iso- dimethyl form in ES degraded final hydrocarbon product. The band observed at 1364 cm^{-1} corresponds to *gauche* conformation with methyl groups in gem-form. While the 1379 cm^{-1} peak component arises from $-CH_3$ iso- form umbrella mode. The medium intensity for this mode confirms both crystalline and amorphous phases in ES-GNP solution.

$-SO_3$ Vibrational modes

A-component and *E*- component of $\nu-SO_3$ asymmetric (ν_{asym}) and symmetric (ν_{sym}) stretching modes of $-SO_3$ functional group are observed in the ES spectrum at 1269 and 1245 cm^{-1} respectively. The intensity of 1269 cm^{-1} band is more than 1245 cm^{-1}, due to strong in-plane hydrogen bond interaction between sulphite

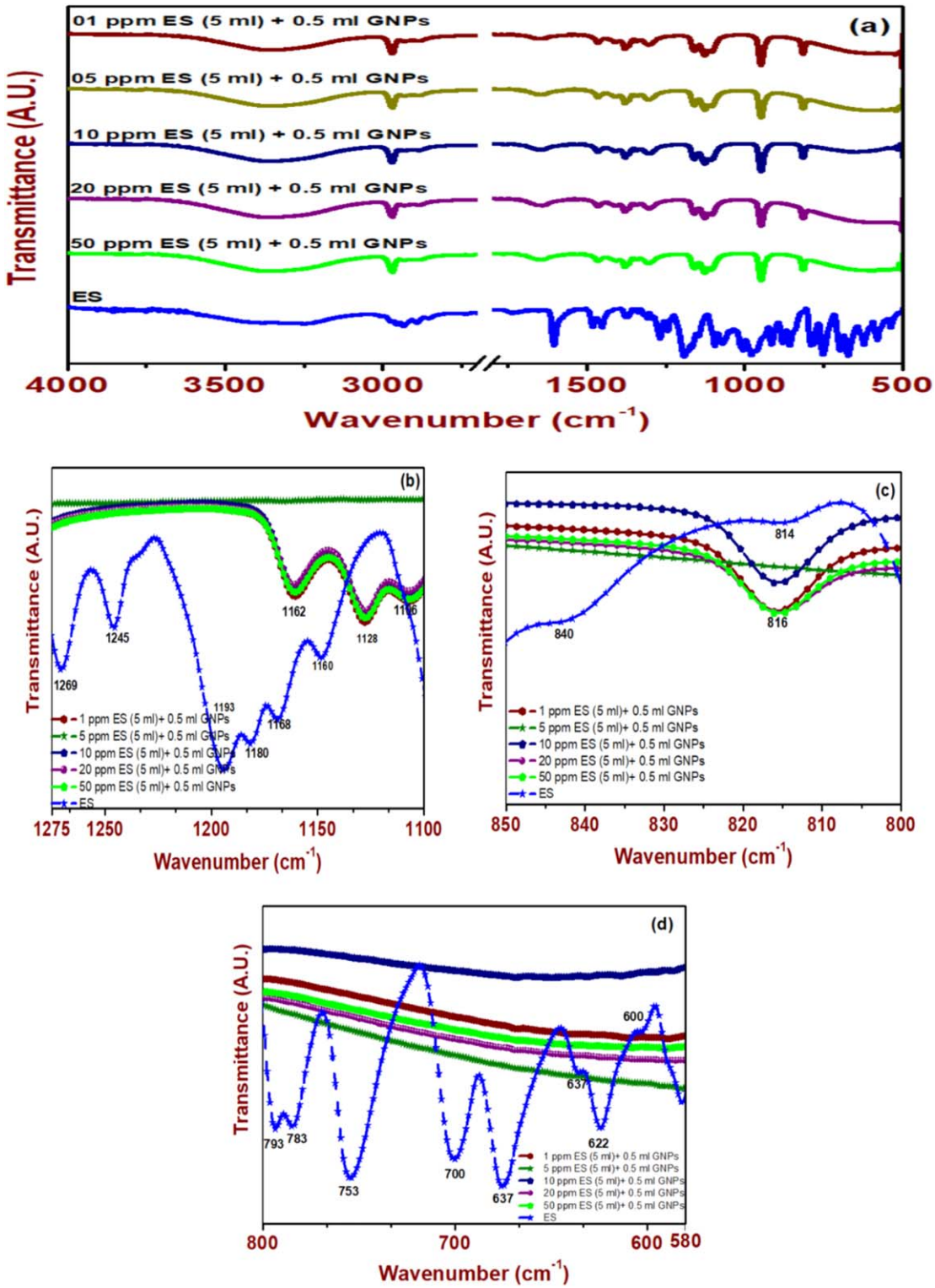

Figure 7. (a) IR transmittance spectra of x ppm ES (5 ml) (x = 1, 5, 10, 20, 50 ppm) solutions treated with 0.5 ml GNPs in 4000–500 cm^{-1} region with Zoomed-in views of (b) 1275–1100 cm^{-1}, (c) 850–800 cm^{-1} and (d) 800–580 cm^{-1} regions.

oxygen and propanol –OH functional group hydrogen atom as compared to their lateral interactions between ES molecules. ν–SO_2 asymmetrical stretching mode is obtained as strong peak at 1095 cm^{-1} along with medium intensity peak at 1072 cm^{-1} and very weak intensity component at 1043 cm^{-1}. The symmetrical stretching modes of –SO_2 group appear as strong bands at 1006 and 981 cm^{-1} [41]. While its bending modes are observed as medium intensity peaks at 538 and 508 cm^{-1} in ES. These peaks disappear in GNPs treated ES solutions IR transmittance spectra which confirms the degradation of ES sulphite group with GNPs treatment.

C–H bending, CH_3 rocking and C–H wagging vibrations

The very strong broad transmittance peak in 1225–1100 cm^{-1} region with components at (1193, 1145) cm^{-1} and (1180, 1168) cm^{-1} pertains to C–H bend. and CH_3 rock modes respectively in ES IR transmittance spectrum. While in GNPs treated ES solutions, three peak components are observed at 1162, 1128 and 1106 cm^{-1}, as shown in figure 7(b) (Zoomed-in view of 1275–1100 cm^{-1} region). C–H_{wagg}. mode appears as shoulder band with component and medium intensity peak at (840 and 814) cm^{-1} and 816 cm^{-1} respectively in IR transmittance spectra of ES and GNPs treated ES solutions (figure 7(c)).

$C–C_{stretch.}$, $C–O_{stretch.}$ and $O–C_{stretch.}$ vibrations

$\nu C–C_{stretch.}$ modes are observed as shoulder bands at 966 and 940 cm^{-1} in ES and as a very strong peak at 950 cm^{-1} in GNPs treated ES solutions IR spectra. $\nu C–O_{stretch}$ and $\nu O–C_{stretch}$. modes are obtained as medium intensity peaks at 917, 880, 858 cm^{-1} in ES and in GNPs treated ES final solutions, these peaks disappeared. This confirms the degradation of oxygen bonded carbon functional groups in ES molecule.

C–Cl stretching vibrations

In ES, six C–Cl bonds are present in three different environments labelled as 1a, 1b, 2a, 2b, 3a and 3b. νC–Cl stretching modes of these $–C(Cl)_2$ and Cl–C=C–Cl groups are obtained at (793, 783), 754, 700, 673, (637, 622, 600), 582 cm^{-1} in pure ES IR spectra figure 7(d) (in zoomed view of 800–580 cm^{-1} region). These peak disappear in GNPs treated ES solutions due to photocatalytic reductive dechlorination reaction in which all the chlorine bonded groups degrade simultaneously.

IR spectroscopic studies revealed the complete degradation of ES on treatment with GNPs as evidenced from the disappearance of carbonyl, $–SO_3$ and C–Cl functional groups vibrational peaks observed in 1275–1150 cm^{-1}, 850–800 cm^{-1} and 800–580 cm^{-1} regions respectively.

Proposed mechanism

The use of noble metal nanoparticles (NPs) as a photocatalyst has many advantages like high optical absorption in the visible region of solar spectrum, no band gap and the availability of large number of high energy electrons at their surface to initiate chemical reaction with adsorbed molecules [19, 20, 22, 48–55]. In GNPs, most of the conduction electrons (6sp states) are present at the surface of NPs and very small number of them are distributed above Fermi levels. At ambient condition, GNPs absorb both visible and UV components from normal sunlight simultaneously due to LSPR and inter-band transitions between 5d and 6sp states. The conduction electrons gain the energy of light irradiation and distribute large number of conduction electrons to high energy levels. The availability of such high energy electrons (hot electrons) at the surface of GNPs are suitable for the degradation of ES molecules adsorbed on their surface by the oxidation, reduction and hydrolysis chemical reactions. The schematic of the proposed mechanism is shown in the following figure 8.

In the present investigations, the degradation of commercial grade ES solutions in varied concentrations using GNPs is discussed in the light of phototcatalytic activity of GNPs. Based on the earlier reported ES degradation pathways, we exploited the probable photochemical process in the current studies. ES sulphite functional group hydrolyses to form less toxic endosulfan diol [16] which oxidises to endosulfan ether to endosulfan hydroxyl carboxylic acid/endosulfan lactone and endosulfan hydroxyether. The intermediate reaction products finally mineralize to sulphur dioxide and carbon dioxide. The mineralization of carcinogenic ES chlorinated skeleton ring takes place by reductive dechlorination reaction [56–60]. Very fast reductive reaction removes all six chlorine atoms labelled as 1a/1b, 2a/2b, 3a/3b simultaneously as Cl_2 gas. The proposed mechanism is supported by TEM, UV–Vis and FTIR studies. The mineralization chemical reaction pathway is also given below (figure 9).

Conclusion

The results presented in this study provide definitive evidence for the mineralization of ES pesticide by photocatalytic GNPs. TEM, optical absorption and FTIR analytical techniques were used to confirm the nearly complete degradation of ES pesticide. Based upon the results derived from morphological, optical absorption and IR transmittance spectra of GNPs colloidal solution treated ES (1, 5, 10, 20 and 50 ppm) solutions, ES degradation via intermediate hydrolysis, oxidation and reduction reaction mechanism has been proposed. The agglomeration of GNPs into small and big ensembles bring visible change in colloidal solution coloration. TEM images confirm the agglomeration of GNPs into different patterns whose size varies from few micrometer to millimetre. Optical absorption spectra of GNPs treated ES solutions show peaks pertaining to the inter-band, LSPR of individual and clustered GNPs in UV and visible regions with the variation in peaks intensity. IR

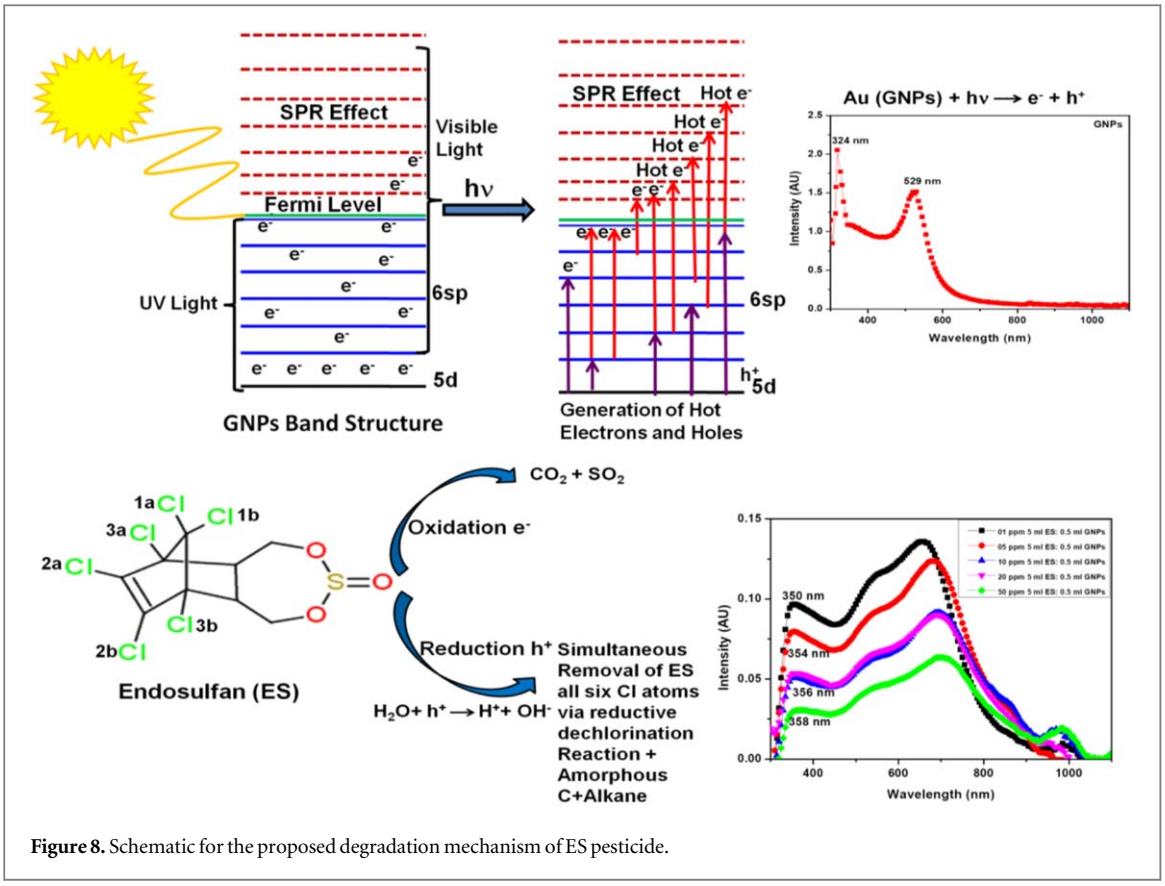

Figure 8. Schematic for the proposed degradation mechanism of ES pesticide.

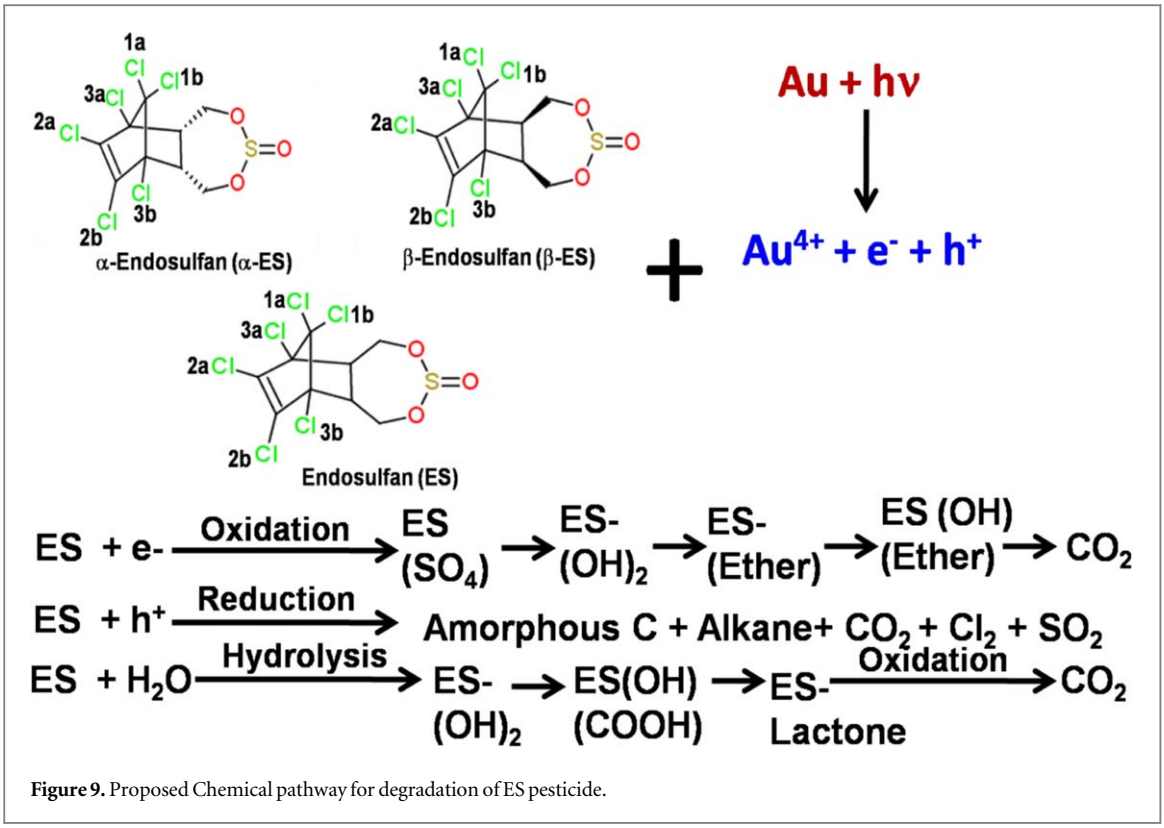

Figure 9. Proposed Chemical pathway for degradation of ES pesticide.

transmittance spectra also reveal the nearly complete disintegration of ES pesticide by the formation of amorphous carbon and hydrocarbons as final reaction products. Hence, novel GNPs are found to be a suitable and efficient photocatalyst for providing an easy and swift way to eradicate highly persistent toxic ES pesticide from the environment with a zero waste.

Acknowledgments

The authors sincerely thank Vice Chancellor, GB Pant University of Agriculture and Technology for continuous encouragement and interest in this work.

Individual author contribution

Puja Goel: Planning and execution of experiment, data analysis and manuscript writing.
Manju Arora: In depth IR analysis and manuscript writing.

ORCID iDs

Puja Goel https://orcid.org/0000-0002-4385-2356

References

[1] Bolton J R and Cater S R 1994 Homogeneous photodegradation of pollutants in contaminated water: an introduction *Aquatic and Surface Photochemistry* ed G R Helz, R G Zepp and D G Crosby (Boca Raton, FL: Lewis) Chapter 33 pp 467–90
[2] Linsebigler A L, Lu G and Yates J T Jr 1995 Photocatalysis on TiO_2 surfaces: principles, mechanisms, and selected results *Chem. Rev.* **95** 735–58
[3] Navarro S, Fenoll J, Vela N, Ruiz E and Navarro G 2009 Photocatalytic degradation of eight pesticides in leaching water by use of ZnO under natural sunlight *J. Hazard. Mater.* **172** 1303–10
[4] Hu J S, Ren L L, Guo Y G, Liang H P, Cao A M, Wan L J and Bai C L 2005 Mass production and high photocatalytic activity of ZnS nanoporous nanoparticles *Angew. Chem. Int. Ed.* **117** 1295–1299.
[5] Hernandez-Uresti D B, Sánchez-Martínez D, Martínez-de la Cruz A, Sepúlveda-Guzmán S and Torres-Martínez L M 2014 Characterization and photocatalytic properties of hexagonal and monoclinic WO_3 prepared via microwave-assisted hydrothermal synthesis *Ceram. Int.* **40** 4767–75
[6] Sood S, Umar A, Mehta S K and Kansal S K 2015 α- Bi_2O_3 nanorods: an efficient sunlight active photocatalyst for degradation of rhodamine B and 2,4,6-trichlorophenol *Ceram. Int.* **41** 3355–64
[7] Ayodhya D and Veerabhadram G 2017 Investigation of structural, optical, catalytic, fluorescence studies of eco-friendly synthesized Bi_2S_3 nanostructures *Superlattices Microstruct.* **102** 103–18
[8] Wang M, Gao Y, Dai L, Cao C, Chen Z and Guo X 2013 Surfactant free hydrothermal synthesis of SnO_2 powders with controllable morphologies and their photocatalytic water treatment application *Sci. Adv. Mater.* **5** 1867–76
[9] Zhang G, Yan Y, Song L, Yue Q, Qu F and Zhang X 2012 Facile synthesis of mesoporous MnO_2 flower-like nanostructures and their catalytic performance in the degradation of Poly(ethylene terephthalate) wastes *Sci. Adv. -23- Mater.* **4** 1179–84
[10] Mishra N K (ed) 2016 *Catalytic Application of Nano-Gold Catalysts* (Croatia: Intech Open) (https://doi.org/10.5772/61954)
[11] Jing Q, Feng X, Zhao X, Duan Z, Pan J, Chen L and Liu Y 2018 Bi/$BiVO_4$ chain-like hollow microstructures: synthesis, characterization and application as visible-light-active photocatalysts *ACS Appl. Nano Mater.* **1** 2653–61
[12] Li T, Wang Y, He Y, Cai J, Luo M and Zhao L 2012 Preparation and photocataytic property of $Sr_{0.25}Bi_{0.75}O_{1.36}$photocatalyst *Mater. Lett.* **74** 170–2
[13] Priyadharsan A, Vasanthakumar V, Karthikeyan S, Raj V, Shanavas S and Anbarasan P M 2017 Multi-functional properties of ternary CeO_2/SnO_2/rGO nanocomposites: visible light driven photocatalyst and heavy metal removal *J. Photochem. Photobiol.* A **346** 32–45
[14] Bi Y, Ouyang S, Umezawa N, Cao J and Ye J 2011 Facet effect of single-crystalline Ag_3PO_4 sub-microcrystals on photocatalytic properties *J. Am. Chem. Soc.* **113** 6490–2
[15] Parveen S, Bhatti I A, Ashar A, Javed T, Mohsin M, Hussain M T, Khan M I, Naz S and Iqbal M 2020 Synthesis, characterization and photocatalytic performance of iron molybdate ($Fe_2(MoO_4)_3$) for the degradation of endosulfan pesticide *Mater. Res. Express* **7** 035016 (12 pages)
[16] Chen S, Ingram R S, Hostetler M J, Pietron J J, Murray R W, Schaaff T G, Khoury J T, Alvarez M M and Whetten R L 1998 Gold nanoelectrodes of varied size: transition to molecule-like charging *Science* **280** 2098–101
[17] Yamada K, Miyajima K and Mafun F 2007 Thermionic emission of electrons from gold nanoparticles by nanosecond pulse-laser excitation of interband *J. Phys. Chem.* C **111** 11246–51
[18] Balamurugan B and Maruyama T 2005 Evidence of an enhanced interband absorption in Au nanoparticles: size-dependent electronic structure and optical properties *Appl. Phys. Lett.* **87** 143105 (4 Pages)
[19] Linic S, Christopher P and Ingram D B 2011 Plasmonic-metal nanostructures for efficient conversion of solar to chemical energy *Nat. Mater.* **10** 911–21
[20] Jain P K and El Sayed M A 2010 Plasmonic coupling in noble metal nanostructures *Chem. Phys. Lett.* **487** 153–64
[21] Xian T, Yang H, Di L J and Dai J F 2015 Enhanced photocatalytic activity of $SrTiO_3$ particles by surface decoration with Ag nanoparticles for dye degradation *Phys. Scripta* **90** 24632469
[22] Zhao J, Nguyen S C, Ye R, Ye B, Weller H, Somorjai G A, Alivisatos A P and Toste F D 2017 A comparison of photocatalytic activities of gold nanoparticles following plasmonic and interband excitation and a strategy for harnessing interband hot carriers for solution phase photocatalysis *ACS Cent. Sci.* **3** 482–8
[23] Nair A S, Tom R T and Pradeep T 2003 Detection and extraction of endosulfan by metal nanoparticles *J. Environ. Monitoring* **5** 363–5
[24] Nair A S and Pradeep T 2003 Halocarbon mineralization and catalytic destruction by metal nanoparticles *Curr. Sci.* **84** 1560–4 ISSN 0011-3891
[25] Bootharaju M S and Pradeep T 2012 Understanding the degradation pathway of the pesticide, chlorpyrifos by noble metal nanoparticles *Langmuir* **28** 2671–9
[26] Goel P and Arora M 2018 Fabrication of chemical sensor for organochlorine pesticide detection using colloidal gold nanoparticles *MRS Commun.* **8** 1000–7

[27] Goel P and Arora M 2020 Remediation of wastewater from chlorpyrifos pesticide by nano-gold photocatalyst *MRS Adv.* 1–7
[28] Xia T, Kovochich M, Brant J, Hotze M, Sempf J, Oberley T, Sioutas C, Yeh J I, Wiesner M R and Nel A E 2006 Comparison of the abilities of ambient and manufactured nanoparticles to induce cellular toxicity according to an oxidative stress paradigm *Nano Lett.* **6** 1794–807
[29] Dreher K L 2004 Health and environmental impact of nanotechnology: toxicological assessment of manufactured nanoparticles *Toxicol. Sci.* **77** 3–5
[30] Turkevich J, Stevenson P C and Hillier J 1951 A study of the nucleation and growth processes in the synthesis of colloidal gold *Discuss. Faraday Soc.* **11** 55–75
[31] Yamada K, Miyajima K and Mafun F 2007 Thermionic emission of electrons from gold nanoparticles by nanosecond pulse-laser excitation of interband *J. Phys. Chem.* C **30** 11246–51
[32] Anguita J V, Silva S R P, Burden A P, Sealy B J, Haq S, Hebbron M, Sturland I and Pritchard A 1999 Thermal stability of plasma deposited thin films of hydrogenated carbon–nitrogen alloys *J. Appl. Phys.* **86** 6276–81
[33] Dischler A, Bubenzer A and Koidl P 1983 Bonding in hydrogenated hard carbon studied by optical spectroscopy *Solid State Commun.* **48** 105–8
[34] Dischler A, Bubenzer A and Koidl P 1983 Hard carbon coatings with low optical absorption *Appl. Phys. Lett.* **42** 636–8
[35] Zhang Q, Rusli H and Ahn J 1998 Influence of oxygen on the thermal stability of amorphous hydrogenated carbon films *J. Appl. Phys.* **83** 1349–1352.
[36] Li Z, Yang Z and Xiao R 1996 2D and 3D graphene nanocomposites: fundamentals, design, and devices *Appl. Phys.* A **63** 243–6
[37] Stief R, Schafer J, Ristein J, Ley L and Beyer W 1996 Hydrogen bonding analysis in amorphous hydrogenated carbon by a combination of infrared absorption and thermal effusion experiments *J. Non-Cryst. Solids* **198** 636–40
[38] Silverstein R M and Webster F X 2003 *Spectrometric Identification of Organic Compounds* 6th edn (United States of America: John Wiley and Sons, Inc.)
[39] Roeges N P G 1994 *A Guide to the Complete Interpretation of IR Spectra of Organic Compounds* (New York: Wiley) 978-0-471-93998-6
[40] Zhang M, Wang P and Nakayama Y 1997 Formation of carbon nitride films by the radio-frequency plasma chemical vapor deposition method *Japn. J. Appl. Phys.* **36** 4893–6
[41] Wong T C, Wong N B and Tanner P A 1997 A fourier transform IR study of the phase transitions and molecular order in the hexadecyl-trimethyl ammonium sulfate/water system *J. Colloid and Interface Sci.* **186** 325–31
[42] Weers J G and Scheuing D 1991 Structure/performance relationships in monoalkyl/dialkyl cationic surfactant mixtures *J. Colloid and Interface Science* **145** 563–80
[43] Snyder R G 1967 Syntheses and physical studies of inorganic compounds *J. Chem. Phys.* **47** 1316–60
[44] Ferrari A C, Rodil S E and Robertson J 2003 Interpretation of infrared and raman spectra of amorphous carbon nitrides *Phys. Rev.* B **67** 155306 (20 Pages)
[45] Knoll J and Geiger J 1984 Optical constants of arc-evaporated amorphous carbon in the far-infrared spectral region *Phy. Rev.* B **29** 5651–5
[46] Bonelli M, Ferrari A C, Fioravanti A, Li Bassi A, Miotello A and Ossi P M 2002 Structure and mechanical properties of low stress tetrahedral amorphous carbon films prepared by pulsed laser deposition *Euro. Phys. J.* B **25** 269–80
[47] Burstein E, Brodsky M H and Lucovsky G 1967 The dynamic ionic charge of zinc blende type crystals *Int. J. Quantum Chem.* **1S** 759–65
[48] Kamat P V 2002 Photophysical, photochemical and photocatalytic aspects of metal nanoparticles *J. Phys. Chem.* B **106** 7729–44
[49] Kelly K L, Coronado E, Zhao L L and Schatz G C 2003 The optical properties of metal nanoparticles: the influence of size, shape, and dielectric environment *J. Phys. Chem.* B **107** 668 - 677
[50] Cushing S K, Li J T, Meng F, Senty T R, Suri S, Zhi M J, Li M, Bristow A D and Wu N Q 2012 Photocatalytic activity enhanced by plasmonic resonant energy transfer from metal to semiconductor *J. Am. Chem. Soc.* **134** 15033–15044.
[51] Watanabe K, Menzel D, Nilius N and Freund H J 2006 Photochemistry on metal nanoparticles *Chem. Rev.* **106** 4301–20
[52] Zhu H Y, Chen X, Zheng Z F, Ke X B, Jaatinen E and Zhao J C 2009 Mechanism of supported gold nanoparticles as photocatalysts under ultraviolet and visible light irradiation *Chem. Commun.* **48** 7524–6
[53] Nehl C L and Hafner J H 2008 Shape-dependent plasmon resonances of gold nanoparticles *Mater J. Chem.* **18** 2415–9
[54] Brongersma M L, Halas N J and Nordlander P 2015 Plasmon-induced hot carrier science and technology *Nat. Nanotechnol.* **10** 25–34
[55] Devipriya S and Yesodharan S 2005 Colloids for nano- and biotechnology *Sol. Cells* **86** 309–48
[56] Singh S P and Bose P 2017 Reductive dechlorination of endosulfan isomers and its metabolites by zero-valent metals: reaction mechanism and degradation products *RSC Adv.* **7** 27668–77
[57] Arnold W A and Roberts A L 2000 Pathways and kinetics of chlorinated ethylene and chlorinated acetylene reaction with Fe(0) particles *Environ. Sci. Technol.* **34** 1794–805
[58] Elsner M, Haderlein S B, Kellerhals T, Luzi S, Zwank L, Angst W and Schwarezenbach R P 2004 Mechanisms and products of surface-mediated reductive dehalogenation of carbon tetrachloride by Fe(II) on goethite *Environ. Sci. Technol.* **38** 2058–66
[59] Roberts A L, Totten L A, Arnold W A, Burris D R and Campbell T J 1996 Reductive elimination of chlorinated ethylenes by zero-valent metals *Environ. Sci. Technol.* **30** 2654–9
[60] Bylaska E J, Dupuis M and Tratnyek P G 2008 One-electron-transfer reactions of polychlorinated ethylenes: concerted and stepwise cleavages *J. Phys. Chem.* A **112** 3712–21